Quantitatively extracting the contribution of asymmetric local-field to $\chi^{(2)}$ in cross-shaped Ag nanoholes

Jiawei Chen,[1] Kai Wang,[1,*] Hua Long,[1] Hongbo Hu,[1] Xiaobo Han,[1] Bing Wang,[1] and Peixiang Lu[1,2]

[1]*Wuhan National Laboratory for Optoelectronics and School of Physics, Huazhong University of Science and Technology, Wuhan 430074, China*
[2]*Laboratory for Optical Information Technology, Wuhan Institute of Technology, Wuhan 430205, China*
*kale_wong@hust.edu.cn

Abstract: We systematically study the contribution of local-field distribution to second-harmonic generation (SHG) in cross-shaped Ag nanohole arrays, which is usually covered by resonance enhancement effect. By increasing one arm-length of the centrosymmetric cross-shaped Ag nanohole, the local-field distribution varies from centrosymmetric to non-centrosymmetric, while the localized surface plasmon resonance peak is red-shifted to the wavelength of the pumping laser accordingly. Both experimental and stimulated results indicate that the contribution of the asymmetric local-field distribution to SHG is quantitatively separated from a strong resonance enhancement effect. It shows that the pure effective second-order nonlinear susceptibility increases as the asymmetric degree of local-field distribution increases, and the largest effective second-order nonlinear susceptibility is ~2.5 times to that in a centrosymmetric local-field distribution. Our results provide evidence for optimizing the design of nonlinear plasmonic nanoantennas and metasurfaces.

References and links

1. S. A. Maier, *Plasmonics: Fundamentals and Applications* (Springer, 2007).
2. E. Hutter and J. H. Fendler, "Exploitation of localized surface plasmon resonance," Adv. Mater. **16**(19), 1685–1706 (2004).
3. J. N. Anker, W. P. Hall, O. Lyandres, N. C. Shah, J. Zhao, and R. P. Van Duyne, "Biosensing with plasmonic nanosensors," Nat. Mater. **7**(6), 442–453 (2008).
4. S. Ke, B. Wang, H. Huang, H. Long, K. Wang, and P. Lu, "Plasmonic absorption enhancement in periodic cross-shaped graphene arrays," Opt. Express **23**(7), 8888–8900 (2015).
5. N. Fang, H. Lee, C. Sun, and X. Zhang, "Sub-diffraction-limited optical imaging with a silver superlens," Science **308**(5721), 534–537 (2005).
6. V. G. Kravets, F. Schedin, R. Jalil, L. Britnell, R. V. Gorbachev, D. Ansell, B. Thackray, K. S. Novoselov, A. K. Geim, A. V. Kabashin, and A. N. Grigorenko, "Singular phase nano-optics in plasmonic metamaterials for label-free single-molecule detection," Nat. Mater. **12**(4), 304–309 (2013).
7. H. A. Atwater and A. Polman, "Plasmonics for improved photovoltaic devices," Nat. Mater. **9**(3), 205–213 (2010).
8. M. Kauranen and A. V. Zayats, "Nonlinear plasmonics," Nat. Photonics **6**(11), 737–748 (2012).
9. J. F. Li, Y. F. Huang, Y. Ding, Z. L. Yang, S. B. Li, X. S. Zhou, F. R. Fan, W. Zhang, Z. Y. Zhou, D. Y. Wu, B. Ren, Z. L. Wang, and Z. Q. Tian, "Shell-isolated nanoparticle-enhanced Raman spectroscopy," Nature **464**(7287), 392–395 (2010).
10. X. Wen, G. Li, J. Zhang, Q. Zhang, B. Peng, L. M. Wong, S. Wang, and Q. Xiong, "Transparent free-standing metamaterials and their applications in surface-enhanced Raman scattering," Nanoscale **6**(1), 132–139 (2014).
11. W. Cai, A. P. Vasudev, and M. L. Brongersma, "Electrically controlled nonlinear generation of light with plasmonics," Science **333**(6050), 1720–1723 (2011).
12. H. Aouani, M. Rahmani, M. Navarro-Cía, and S. A. Maier, "Third-harmonic-upconversion enhancement from a single semiconductor nanoparticle coupled to a plasmonic antenna," Nat. Nanotechnol. **9**(4), 290–294 (2014).
13. H. Harutyunyan, G. Volpe, R. Quidant, and L. Novotny, "Enhancing the nonlinear optical response using multifrequency gold-nanowire antennas," Phys. Rev. Lett. **108**(21), 217403 (2012).
14. W. Liu, K. Wang, Z. Liu, G. Shen, and P. Lu, "Laterally emitted surface second harmonic generation in a single ZnTe nanowire," Nano Lett. **13**(9), 4224–4229 (2013).

15. H. Linnenbank and S. Linden, "Second harmonic generation spectroscopy on second harmonic resonant plasmonic metamaterials," Optica **2**(8), 698–701 (2015).
16. L. J. Black, P. R. Wiecha, Y. Wang, C. H. de Groot, V. Paillard, C. Girard, O. L. Muskens, and A. Arbouet, "Tailoring second-harmonic generation in single L-shaped plasmonic nanoantennas from the capacitive to conductive coupling regime," ACS Photonics **2**(11), 1592–1601 (2015).
17. B. K. Canfield, H. Husu, J. Laukkanen, B. Bai, M. Kuittinen, J. Turunen, and M. Kauranen, "Local field asymmetry drives second-harmonic generation in non-centrosymmetric nanodimers," Nano Lett. **7**(5), 1251–1255 (2007).
18. R. Czaplicki, J. Mäkitalo, R. Siikanen, H. Husu, J. Lehtolahti, M. Kuittinen, and M. Kauranen, "Second-harmonic generation from metal nanoparticles: Resonance enhancement versus particle geometry," Nano Lett. **15**(1), 530–534 (2015).
19. V. K. Valev, A. V. Silhanek, N. Verellen, W. Gillijns, P. Van Dorpe, O. A. Aktsipetrov, G. A. Vandenbosch, V. V. Moshchalkov, and T. Verbiest, "Asymmetric optical second-harmonic generation from chiral G-shaped gold nanostructures," Phys. Rev. Lett. **104**(12), 127401 (2010).
20. K. Thyagarajan, J. Butet, and O. J. Martin, "Augmenting second harmonic generation using Fano resonances in plasmonic systems," Nano Lett. **13**(4), 1847–1851 (2013).
21. J. A. van Nieuwstadt, M. Sandtke, R. H. Harmsen, F. B. Segerink, J. C. Prangsma, S. Enoch, and L. Kuipers, "Strong modification of the nonlinear optical response of metallic subwavelength hole arrays," Phys. Rev. Lett. **97**(14), 146102 (2006).
22. K. Konishi, T. Higuchi, J. Li, J. Larsson, S. Ishii, and M. Kuwata-Gonokami, "Polarization-controlled circular second-harmonic generation from metal hole arrays with threefold rotational symmetry," Phys. Rev. Lett. **112**(13), 135502 (2014).
23. N. Segal, S. Keren-Zur, N. Hendler, and T. Ellenbogen, "Controlling light with metamaterial-based nonlinear photonic crystals," Nat. Photonics **9**(3), 180–184 (2015).
24. S. D. Liu, E. S. Leong, G. C. Li, Y. Hou, J. Deng, J. H. Teng, H. C. Ong, and D. Y. Lei, "Polarization-independent multiple Fano resonances in plasmonic nanomers for multimode-matching enhanced multiband second-harmonic generation," ACS Nano **10**(1), 1442–1453 (2016).
25. J. M. Yi, V. Smirnov, X. Piao, J. Hong, H. Kollmann, M. Silies, W. Wang, P. Groß, R. Vogelgesang, N. Park, and C. Lienau, "Suppression of radiative damping and enhancement of second harmonic generation in bull's eye nanoresonators," ACS Nano **10**(1), 475–483 (2016).
26. Y. Zhang, N. K. Grady, C. Ayala-Orozco, and N. J. Halas, "Three-dimensional nanostructures as highly efficient generators of second harmonic light," Nano Lett. **11**(12), 5519–5523 (2011).
27. H. Aouani, M. Navarro-Cia, M. Rahmani, T. P. Sidiropoulos, M. Hong, R. F. Oulton, and S. A. Maier, "Multiresonant broadband optical antennas as efficient tunable nanosources of second harmonic light," Nano Lett. **12**(9), 4997–5002 (2012).
28. J. Berthelot, G. Bachelier, M. Song, P. Rai, G. Colas des Francs, A. Dereux, and A. Bouhelier, "Silencing and enhancement of second-harmonic generation in optical gap antennas," Opt. Express **20**(10), 10498–10508 (2012).
29. J. Butet, P. F. Brevet, and O. J. Martin, "Optical second harmonic generation in plasmonic nanostructures: From fundamental principles to advanced applications," ACS Nano **9**(11), 10545–10562 (2015).
30. J. Butet and O. J. Martin, "Evaluation of the nonlinear response of plasmonic metasurfaces: Miller's rule, nonlinear effective susceptibility method, and full-wave computation," J. Opt. Soc. Am. B **33**(2), A8–A15 (2016).
31. A. Slablab, L. Le Xuan, M. Zielinski, Y. de Wilde, V. Jacques, D. Chauvat, and J. F. Roch, "Second-harmonic generation from coupled plasmon modes in a single dimer of gold nanospheres," Opt. Express **20**(1), 220–227 (2012).
32. M. Celebrano, X. Wu, M. Baselli, S. Großmann, P. Biagioni, A. Locatelli, C. De Angelis, G. Cerullo, R. Osellame, B. Hecht, L. Duò, F. Ciccacci, and M. Finazzi, "Mode matching in multiresonant plasmonic nanoantennas for enhanced second harmonic generation," Nat. Nanotechnol. **10**(5), 412–417 (2015).
33. L. Lin, X. M. Goh, L. P. McGuinness, and A. Roberts, "Plasmonic lenses formed by two-dimensional nanometric cross-shaped aperture arrays for Fresnel-region focusing," Nano Lett. **10**(5), 1936–1940 (2010).
34. H. Hu, K. Wang, H. Long, W. Liu, B. Wang, and P. Lu, "Precise determination of the crystallographic orientations in single ZnS nanowires by second-harmonic generation microscopy," Nano Lett. **15**(5), 3351–3357 (2015).
35. P. Mühlschlegel, H. J. Eisler, O. J. Martin, B. Hecht, and D. W. Pohl, "Resonant optical antennas," Science **308**(5728), 1607–1609 (2005).
36. B. L. Wang, R. Wang, R. J. Liu, X. H. Lu, J. Zhao, and Z. Y. Li, "Origin of shape resonance in second-harmonic generation from metallic nanohole arrays," Sci. Rep. **3**, 2358 (2013).
37. V. Mizrahi and J. E. Sipe, "Phenomenological treatment of surface second-harmonic generation," J. Opt. Soc. Am. B **5**(3), 660–667 (1988).
38. K. O'Brien, H. Suchowski, J. Rho, A. Salandrino, B. Kante, X. Yin, and X. Zhang, "Predicting nonlinear properties of metamaterials from the linear response," Nat. Mater. **14**(4), 379–383 (2015).
39. C. Qin, B. Wang, H. Long, K. Wang, and P. Lu, "nonreciprocal phase shift and mode modulation in dynamic graphene waveguides," J. Lightwave Technol. **34**(16), 3877–3883 (2016).

40. S. Ke, B. Wang, C. Qin, H. Long, K. Wang, and P. Lu, "Exceptional points and asymmetric mode switching in plasmonic waveguides," J. Lightwave Technol. **34**(22), 5258–5262 (2016).
41. E. D. Palik, *Handbook of Optical Constants of Solids* (Academic, 1998), Vol. 3.
42. S. Roke, M. Bonn, and A. V. Petukhov, "Nonlinear optical scattering: The concept of effective susceptibility," Phys. Rev. B **70**(11), 115106 (2004).

1. Introduction

Localized surface plasmon resonances (LSPRs), arising from the interaction of light with noble metal nanostructures, can be described as the collective oscillations of free conduction electrons [1]. It sensitively depends on the size and shape of nanostructures [2–4] and leads to a strong enhancement of local electromagnetic fields, which shows potential applications in super-resolution imaging [5], single molecule detection [6] and light harvesting [7]. In the past decade, LSPRs in noble metal nanostructures have been combined with nonlinear optics that brings a new concept named "nonlinear plasmonics" [8]. Many nonlinear processes can be boosted based on the strong local-field enhancement, including Raman scattering [9,10], second- and third-harmonic generation (SHG and THG) [11,12] and four-wave mixing [13].

SHG is a fundamental and important nonlinear optical effect that converts two photons at a fundamental frequency into one photon at the doubled frequency [14]. As previously reported, the SHG properties in kinds of noble metal nanostructures have been investigated, such as L-shaped [15,16], T-shaped [17,18] and G-shaped nanoparticles [19], oligomers [20], nanoholes [21,22], and even more complicated shapes [23–27]. Most people are concerned about high SHG conversion efficiency in well-designed plasmonic nanostructures by resonance enhancement. However, SHG is limited by the non-centrosymmetry requirement of the material structure as the nature of even-order optical nonlinearity, leading to a rather weak SHG signal in centrosymmetric nanostructures even in the strong resonance condition [28,29]. Furthermore, as recent work reported by Kauranen et al., the SHG responses are still very weak when the local-field distribution is centrosymmetric even though the nanoparticle geometry is non-centrosymmetric [18]. Therefore, the asymmetric local-field distribution plays an important role for a sufficient SHG in plasmonic nanostructures. The local-field distributions can be tailored by the nanostructures geometry, which leads to the variations of second-order nonlinear susceptibility [30]. Since the resonance enhancement effect is usually prominent, this relatively small contribution from the asymmetric local-field distribution is easily neglected or covered by the strong resonance enhancement factors [31,32]. It is therefore a complicated and crucial question to distinguish the influence of the asymmetric local-field distributions from the resonance enhancement effect and make a compromise between these two effects, which is essential in optimizing the designs of nonlinear plasmonic nanoantennas and metasurfaces.

In this paper, we present a quantitative study on the contribution of asymmetric local-field to second-order nonlinear susceptibility $\chi^{(2)}$ in cross-shaped Ag nanohole. By increasing one arm-length of the centrosymmetric cross-shaped Ag nanohole, the local-field distribution varies from centrosymmetric to non-centrosymmetric. At the same time, the associated LSPR peak is red-shifted to the wavelength of pumping laser, leading to a strong local-field enhancement effect that covers the contribution of asymmetric local-field. The experimental results show that the contribution of asymmetric local-field can be quantitatively extracted from the strong resonance enhancement effect by a white-light supercontinuum signal, which is supported by a theoretical calculation based on nonlinear scattering theory. The pure effective $\chi^{(2)}$ is demonstrated to increase as the asymmetric degree of local-field distribution increases, and the largest effective $\chi^{(2)}$ is ~2.5 times to that in a centrosymmetric local-field distribution. Our result quantitatively illustrates the importance of asymmetric local-field to $\chi^{(2)}$, which provides a new evidence for the nonlinear plasmonics design in metal nanostructures.

2. Experimental method

The high-quality silver (Ag) film of 200-nm thickness with a 3-nm thick Cr adhesion layer was deposited onto fused silica substrate by means of magnetron sputtering method. A 26×26 square-lattice array of cross-shaped nanoholes [33] was milled on the film by means of focused ion beam milling method (FIB, FEI Versa 3D), with a spatial periodicity of 400 nm and a total area of $10 \times 10\ \mu m^2$. The transmission spectra of Ag nanohole arrays were measured by a white light source with a linear film polarizer (Thorlabs, SLS201 and LPVIS050). The SHG properties of Ag nanohole arrays were studied by a conventional confocal microscope system at room temperature [34]. A femtosecond laser with a center wavelength at $\lambda = 790$ nm (Spectra Physics, Ti: sapphire laser, 76 MHz) was used as pumping source, and the nonlinear emission spectra were acquired by a spectrometer (Princeton Instruments, Acton 2500i with Pixis 400 CCD camera) in transmission geometry (see Appendix for details).
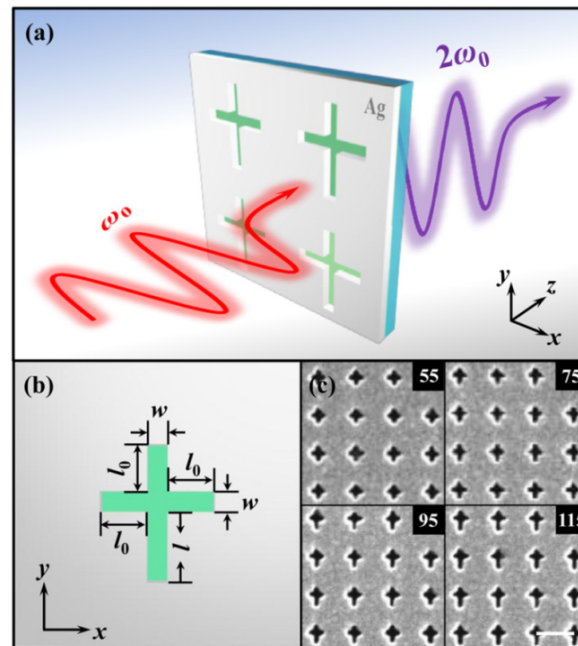
3. Results and discussions

Fig. 1. (a) Illustration of the SHG in the cross-shaped Ag nanohole arrays. Note that the sample is placed in the xy plane with a normal incident laser pumping along z-axis; (b) Geometrical parameters of a single cross-shaped Ag nanohole with the arm-direction along x- and y-axis. The bottom arm-length, l, increases from 55 nm to 115 nm at 10 nm, while the other three arm-length ($l_0 = 55$ nm) and the arm-width ($w = 50$ nm) are kept as constants for all samples; (c) SEM images of four typical cross-shaped Ag nanohole arrays at $l = 55$ nm, 75 nm, 95 nm and 115 nm. The scale bar is 400 nm.

Figure 1(a) shows the experimental scheme that the cross-shaped Ag nanohole arrays are placed in the xy plane under a normal incident laser pumping. Figure 1(b) depicts the corresponding geometrical parameters of a single nanohole with the arm-direction along x- and y-axis. The length of a specific arm (bottom), l, is systematically increased from 55 nm to 115 nm (increased at 10 nm), while the other three arm-lengths, l_0, are kept as a constant of 55 nm. Note that the arm-width, w, is equal to 50 nm for all samples. Figure 1(c) shows the scanning electron microscopy (SEM) images for four typical Ag nanohole arrays at $l = 55$ nm, 75 nm, 95 nm and 115 nm. By the increase of the bottom arm-length (l), the centrosymmetry

of the cross-shaped nanoholes is broken and the asymmetric degree of the nanohole is increased.
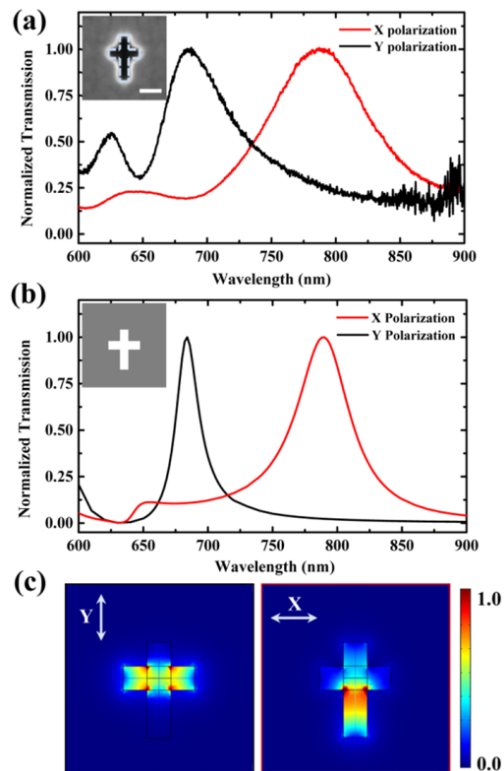

Fig. 2. (a) Measured and (b) simulated transmission spectra for the cross-shaped Ag nanohole arrays at l = 105 nm under x- (red curve) and y-polarized (black curve) illuminations, respectively. The LSPR peaks for x- and y-polarizations are located at 790 nm and 680 nm respectively. The insets show corresponding SEM image of single cross-shaped Ag nanohole as well as a modeled profile. The scale bar is 100 nm; (c) Calculated local-field distribution ($|E|$) under the resonance conditions of x- and y-polarized illuminations by the finite-element solver COMSOL.

The non-centrosymmetry of the cross-shaped nanohole arrays can result in strongly anisotropic optical property, which is further characterized by the transmission spectra measurement. Figure 2(a) presents the measured results of the nanohole array at l = 105 nm under x- (red curve) and y-polarized (black curve) illuminations. Obviously, the x- and y-polarized resonances peaks are located at 790 nm and 680 nm respectively, which can be separated well in spectra. Figure 2(b) shows further simulation results for the same nanohole array by the finite-element solver COMSOL, which is in good agreement with the experimental data. Thus, it is confirmed that cross-shaped Ag nanoholes have strong optical anisotropy, implying rather different LSPR conditions under x- and y-polarized illuminations. The calculated local-field distributions ($|E|$) under the resonance conditions of x- and y-polarized illuminations are shown in Fig. 2(c). The local-field distribution under x-polarized illumination is mainly concentrated in the arms along y-axis, and vice versa. It is therefore demonstrated that the local-field distribution is non-centrosymmetric under x-polarized illumination, while it is centrosymmetric under y-polarized illumination. The variation of local-field distributions can result in quite different second-order nonlinear responses even in the same sample.

The contribution of local field distribution to second-order nonlinear susceptibility $\chi^{(2)}$ is systematically researched by increasing the arm-length l gradually. Figures 3(a) and 3(b) present the measured transmission spectra with the increased arm-length l from 55 nm to 115 nm (increased at 10 nm) under x- and y-polarized illuminations, respectively. As shown in Fig. 3(a),
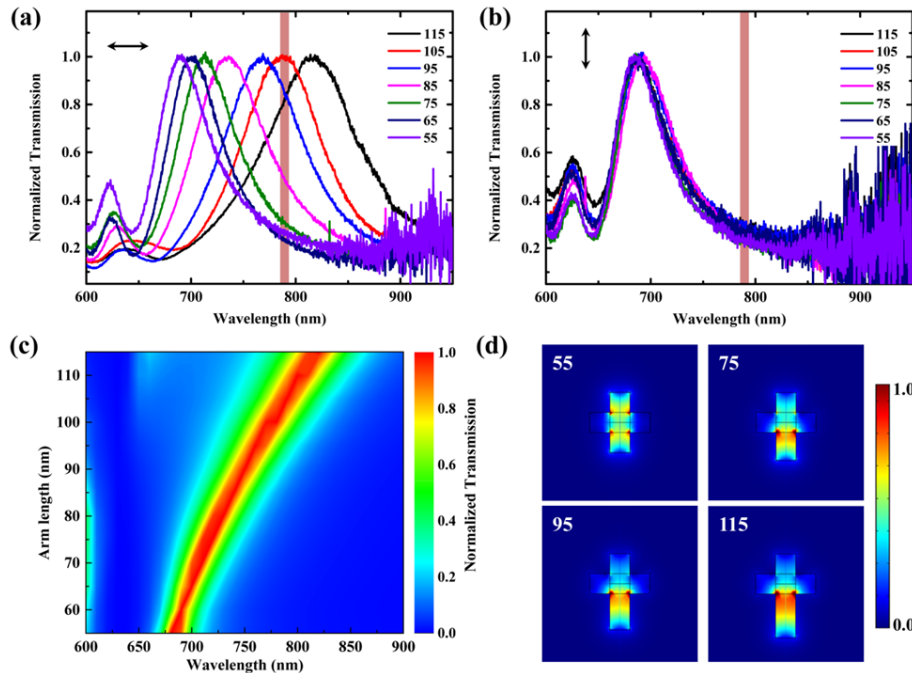

Fig. 3. (a) and (b) Measured transmission spectra with the increased arm-length, l, from 55 nm to 115 nm (increased at 10 nm) under x- and y-polarized illuminations, respectively. The fundamental wavelength of the pumping laser (790 nm) is marked as a vertical dark red bar; (c) Contour plot of the calculated transmission spectra as a function of l under x-polarized light illumination; (d) Corresponding local-field distribution ($|E|$) of four typical samples at l = 55 nm, 75 nm, 95 nm and 115 nm (mentioned in Fig. 1(c)) under x-polarized illumination.

the LSPRs wavelength is remarkably red-shifted under x-polarized illumination as the arm-length increases. However, Fig. 3(b) exhibits that spectra for all samples are approximately the same and no spectral shift can be observed under y-polarized illumination. Accordingly, the local-field distributions for all samples remain centrosymmetric due to the fixed arms along x-axis as shown in Fig. 2(c). Figure 3(c) presents the contour plot featuring calculated transmission spectra as functions of the arm-length l, indicating a good agreement with the experimental results. More importantly, the LSPR peak for the sample at l = 105 nm is spectrally overlapped with the wavelength of the pumping laser at 790 nm, resulting in a strong resonance enhancement effect. Meanwhile, Fig. 3(d) presents the calculated local-field distributions at l = 55 nm, 75 nm, 95 nm and 115 nm under x-polarized illuminations, indicating the significant variations from centrosymmetric to noncentrosymmetric. The increase of the asymmetric degree of local-field distributions is expected to result in a variation of the second-order nonlinear responses of the cross-shaped Ag nanoholes [18].

Figure 4(a) presents measured emission spectra with the increased arm-length l from 55 nm to 115 nm (increased at 10 nm) under x-polarized laser pumping. Generally, it shows a narrowband emission at 395 nm that is exactly the half of the pumping wavelength. Furthermore, it shows quadratic dependency of the signal intensity on the pumping laser intensity, indicating that the signal is generated from a second-order nonlinear process (SHG). It is worth noting that the observed broadband emission is ascribed to white-light

supercontinuum (WLC), which is extended to the detection limit in our experiment (~700 nm). And the WLC signal intensity is proved to be fourth-power of the incident light intensity experimentally (see Appendix for details). Since generated at the interface between the Ag nanoholes and the fused silica substrate [35], the intensity of WLC provides information on the field enhancement at the interface and provides a method to deduct the strong resonance enhancement effect. Figure 4(b) shows the extracted spectra of the WLC signals by high-order polynomial-fitting from the experimental results in Fig. 4(a). A relatively strong WLC signal is obtained when the LSPRs wavelength approaches to the pumping laser, which is ascribed to the strong local field enhancement. The pure SHG signals are acquired by deducting the fitting results of WLC signals (Fig. 4(b)) from the nonlinear emission spectra (Fig. 4(a)), as presented in Fig. 4(c). The inset of Fig. 4(c) shows that the peak intensity of SHG signals varies as a function of the arm-length l, and the largest SHG signal is obtained at $l = 105$ nm which is in perfect resonance with the pumping laser. It indicates ~12.2 times enhancement of SHG intensity in comparison with that in the off-resonant condition at $l = 55$ nm.
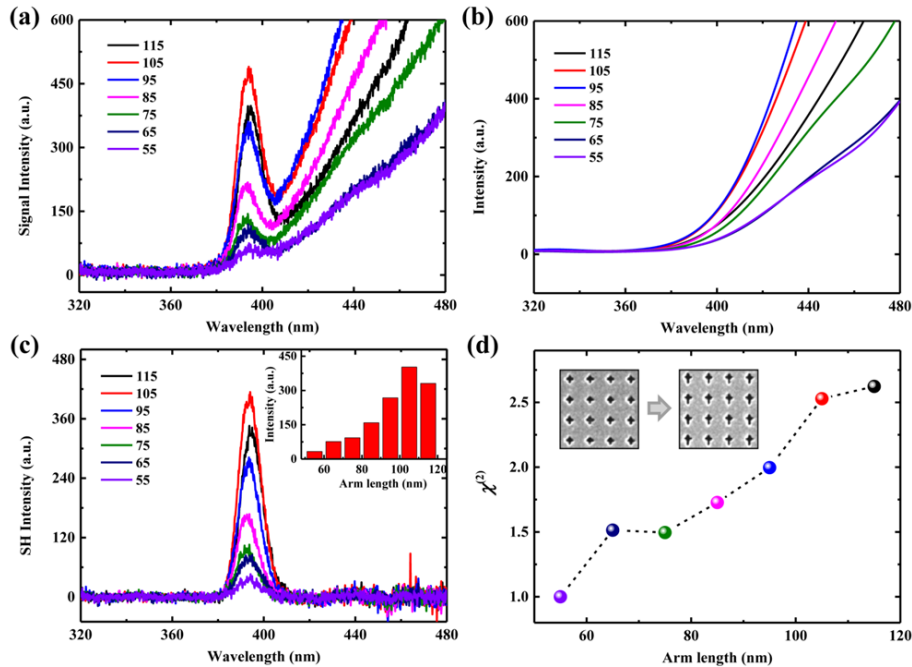

Fig. 4. (a) Measured nonlinear emission spectra of the cross-shaped nanohole arrays with an increased arm-length, l, from 55 nm to 115 nm (increased at 10 nm) under x-polarized laser pumping; (b) The extracted WLC spectra by high-order polynomial-fitting from the results in Fig. 4(a); (c) Acquired SHG signals by deducting the fitting results of WLC signals from the nonlinear emission spectra. The inset shows the SHG intensity as a function of the arm-length l; (d) The normalized effective values of $\chi^{(2)}$ as a function of the arm-length l according to the value of $\chi^{(2)}$ at $l = 55$ nm.

Here the influence of resonance enhancement effect on SHG can be removed by the measured WLC signal. In consideration of a phenomenological field enhancement factor, $L(\omega)$, and an incident fundamental electric field, $E(\omega)$, the enhanced local field amplitude is written as: $E_{\text{loc}}(\omega) = L(\omega)E(\omega)$. Since all samples are in off-resonance with the SH wavelength, the field enhancements by the SH plasmonic mode can be neglected and hence, $L(2\omega) = 1$. In the experiment, the SHG and WLC signals were simultaneously measured, and then the intensities of the emitted SHG and WLC signals are obtained by the following formulas:

$$I_{\text{SHG}} \propto [\chi^{(2)} L^2(\omega) E^2(\omega)]^2, \tag{1}$$

$$I_{\text{WLC}} \propto [L^4(\omega) E^4(\omega)]^2, \tag{2}$$

where $\chi^{(2)} = \chi(2)\,0 + \chi(2)$ asy. $\chi(2)\,0$ originates from the contribution of a few layers of surface atoms in the inner wall of the cross-shaped nanoholes [30,36,37], and $\chi(2)$ asy is from the asymmetric local field distribution. Field enhancement factor, $L(\omega)$, can be extracted from WLC signals and then the second-order susceptibility can be described by:

$$\chi^{(2)} \propto \sqrt{I_{\text{SHG}} / (I_{\text{WLC}})^{1/2}}, \tag{3}$$

where I_{SHG} are taken from the peak values of measured SHG spectra, and I_{WLC} are experimentally estimated by the value at a specific wavelength (480 nm) as the approximate trapezoid-shaped distribution of the broad WLC spectra. The calculated effective values of $\chi^{(2)}$ as a function of arm-length l are presented in Fig. 4(d), which are normalized by the value of $\chi^{(2)}$ at $l = 55$ nm. It clearly indicates that effective values of $\chi^{(2)}$ increases as the growth of asymmetric degree of the cross-shaped nanoholes, which falls in line with the expectation as reported by Zhang's group [38]. In their work, the influence of the resonance enhancement effect is not effectively excluded in calculating second-order nonlinear susceptibility, resulting in the deviation from their expectation.

Since originating from a few layers of surface atoms in the inner wall of nanoholes, $\chi(2)\,0$ remains a constant under the same experiment condition. As a contrast, $\chi(2)$ asy, ascribed to the contribution of the asymmetric local-field distribution, varies as the increase of asymmetric degree of the cross-shaped nanoholes. For the centrosymmetric sample at $l = 55$ nm, $\chi(2)$ asy equals to 0 and thus $\chi^{(2)}$ equals to $\chi(2)\,0$. Therefore, the normalized $\chi^{(2)}$ in Fig. 4(d) represents $\chi(2)$ r = $(\chi(2)\,0 + \chi(2)$ asy$)/\chi(2)\,0 = 1 + \chi(2)$ asy$/\chi(2)\,0$. Then $\chi(2)$ asy = $(\chi(2)$ r - 1$)\chi(2)\,0$. In this way, the contribution of asymmetric local field to $\chi^{(2)}$ is quantitatively extracted in cross-shaped Ag nanoholes after deducting the strong resonance enhancement factor $L(\omega)$ and the intrinsic second-order nonlinear susceptibility $\chi(2)\,0$.

In order to verify the experiment results, the nonlinear responses of the cross-shaped Ag nanoholes were simulated using the finite-element solver COMSOL. In nonlinear scattering theory, the nonlinear emission is described by assuming a local nonlinear susceptibility tensor on the surface of the noble metal. Referred to the method described in [38], the SH electric field is given by the following surface integral:

$$E_{\text{nl}}(2\omega) \propto \iint \chi_{\text{nnn}} E_{\text{n}}^2(\omega) E_{\text{n}}(2\omega) dS, \tag{4}$$

where $E_{\text{nl}}(2\omega)$ is the nonlinear emission, χ_{nnn} is the local nonlinear susceptibility, and $E_{\text{n}}(\omega)$ and $E_{\text{n}}(2\omega)$ are the linear fields of the fundamental mode and the mode at the second harmonic frequency normal to the surface of the nanostructure. The microscopic SH contributions, which are complex valued, add up from each region of the nanostructure, creating constructive or destructive interference in the far-field emission. The calculated fundamental mode and the SH mode are shown in Appendix Fig. 8, and the eventual SH electric field intensity varied as the increased arm-length l is shown in Fig. 5(a). The trend of SH intensity fits well with the experimental results as shown in Fig. 4(c), and the largest enhancement factor of $E(2\omega)$ is 33.6 times at $l = 105$ nm, which is in perfect resonance with the excitation, compared to that of $l = 55$ nm.

Next, we calculated the fundamental field enhancement factor, $L(\omega)$. The enhanced local field amplitude is written as: $E_{\text{loc}}(\omega) = L(\omega)E(\omega)$, where $E(\omega)$ represents the incident fundamental electric field. Actually, in our calculation, $E_{\text{loc}}(\omega)$ and $E(\omega)$ are the integrated values over the whole area containing Ag nanofilms. Normalized $L(\omega)$ varied as the increased arm-length l is shown in Fig. 5(b). The effective second-order susceptibility $\chi^{(2)}$ can be finally calculated based on the following formula:

$$E(2\omega) = \chi^{(2)} L^2(\omega) E^2(\omega). \tag{5}$$

Normalized $\chi^{(2)}$ varied as the increased arm-length l is shown in Fig. 5(c). It can be seen clearly that the largest $\chi^{(2)}$ is not at the same location as the largest $E(2\omega)$ and $L(\omega)$. Instead, it is at about $l = 95$ nm which has the most asymmetrical local-field distribution as shown in Fig. 3(d). When l is smaller than this value, the cross-shaped nanohole approaches to a centro-symmetric geometry and then has a symmetric local-field distribution leading to the small $\chi^{(2)}$. When l is larger than this value, because the local field tends to concentrate in the bottom arm (Fig. 3(d) and extreme case for l to be infinite), it also approaches to a symmetric local-field distribution and results in small $\chi^{(2)}$. Thus, the effective second-order nonlinear susceptibility increases as the asymmetric degree of local-field distribution increases. The largest effective second-order nonlinear susceptibility is ~2.5 times to that in a centrosymmetric local-field distribution. The contribution of asymmetric local field to $\chi^{(2)}$ can be also quantitatively extracted using the aforementioned formula $\chi(2)$ asy = $(\chi(2)$ r - 1$)\chi(2)$ 0.
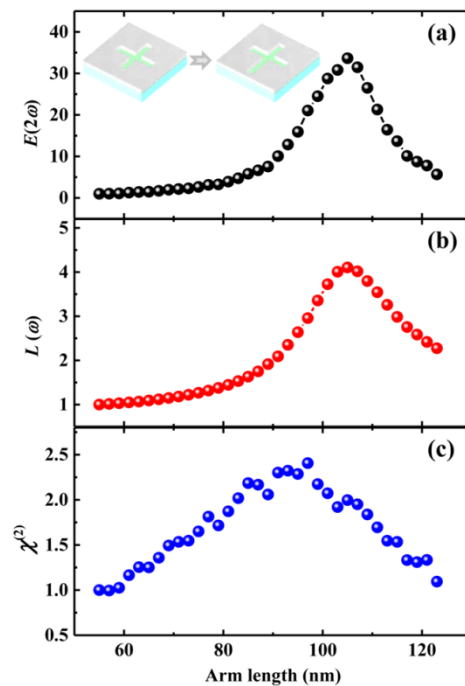

Fig. 5. Calculated (a) SH electric field intensity $E(2\omega)$, (b) fundamental field enhancement factor $L(\omega)$ and (c) effective second-order susceptibility $\chi^{(2)}$ as a function of the arm-length l. They are normalized by the values of $E(2\omega)$, $L(\omega)$ and $\chi^{(2)}$ at $l = 55$ nm, respectively.

Generally, the experimental and simulated results reach a good agreement as l is smaller than 95 nm. Whereas, for $l > 95$ nm, it shows a deviation. This can be interpreted as the local-field distribution in the experiment is not so centrosymmetric as that in the simulation because the fabricated nanoholes have few defects. Then, the symmetry of the local-field distribution still decreases as the increase of the arm-length l at the latter part of the variation, which leads to the continuous increase of $\chi^{(2)}$ in the experiment results.

4. Conclusions

In conclusion, the contribution of asymmetric local field to $\chi^{(2)}$ in cross-shaped Ag nanohole is quantitatively extracted from the strong resonance enhancement effect. By increasing one arm-length of the centrosymmetric cross-shaped Ag nanohole, the local-field distribution varies from centrosymmetric to non-centrosymmetric. At the same time, the localized surface

plasmon resonance peak is red-shifted to the wavelength of the pumping laser. The contribution of asymmetric local-field, $\chi(2)$ asy, is extracted by the calibration of the WLC signal, which is further supported by numerical simulation based on nonlinear scattering theory. $\chi(2)$ asy is demonstrated to increase as the asymmetric degree of local-field distribution increases and the largest effective $\chi^{(2)}$ ($= \chi(2) 0 + \chi(2)$ asy) is ~2.5 times to that in a centrosymmetric local-field distribution. Hence, our results provide clear evidences both in understanding the origins of the enhanced SHG from the plasmonic nanostructures and tailoring the LSPs in the nonlinear plasmonic devices, nanoantennas and metasurfaces for a better performance.

Appendix

A1. The experiment details for the linear and nonlinear optical measurements
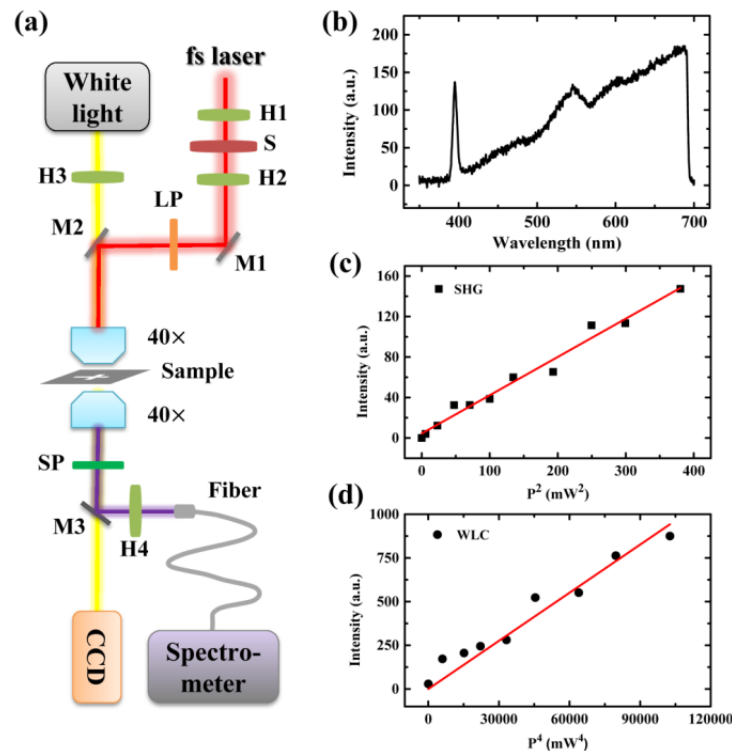

Fig. 6. (a) The schematic sketch of the experiment setup for micro-area transmission and SHG measurements on cross-shaped nanohole arrays. H1, H2: half-wave plates at 800 nm; H3: linear film polarizer; H4: Glan-laser polarizer; S: polarizing beam splitter; LP: 600-nm long pass filter; SP: 720-nm short pass filter. (b) The nonlinear emission spectra of cross-shaped nanohole array with a broad measurement range from 350 to 700 nm. (c) Measured SHG signal intensity I_{SHG} as a function of the square of the pumping power P^2. (d) Measured WLC signal intensity I_{WLC} as a function of the fourth power of the pumping power P^4.

Before performing SH spectroscopy experiments we measured the transmission spectra of the Ag nanohole arrays under normal incidence using a linearly x- or y-polarized white light source (Fig. 6(a)). The white light was from a halogen bulb (Thorlabs, SLS201) and collimated using a polarizer (H3, Thorlabs, LPVIS050) and microscope objective (20×, Olympus, 0.40 NA) in front of the sample. The light after the sample was collected by another identical objective, and subsequently focused to a fiber with a lens and directed to a spectrometer (Princeton Instruments Acton 2500i with Pixis CCD camera). The detection area was selected by the illumination and detection apertures before and after the detecting and

collecting objective. The transmission spectra were normalized with respect to the transmission through a bare fused silica substrate.

The SHG experiment was carried out by a conventional confocal microscope system at room temperature, shown in Fig. 6(a). Stage scanning confocal microscopy allows us to investigate the geometry-dependent nonlinear properties of metamaterials, while avoiding the challenges associated with changing the laser wavelength, such as differences in pulse shape, focal volume size or transmission. A mode-locked Ti-sapphire femtosecond laser system (Tsunami, Spectra-Physics, ~790 nm, 50 fs and 76 MHz) was used as the pumping source. The intensity of the pumping laser beam was adjusted by combining a half-wave plate (H1) and a polarizing beam splitter (S). In addition, the polarization direction of the pumping laser was controlled by another half-wave plate (H2). A microscope objective (40×, Olympus, 0.65 NA) focused the pumping laser onto the sample with a focal spot diameter of ~4 μm. The transmitted nonlinear signal originated from silver nanohole arrays was collected by another identical objective, and subsequently imported to a CCD or spectrometer (Princeton Instruments Acton 2500i with Pixis CCD camera). A 720-nm short-pass filter (SP) filtered out the pumping laser. The polarization-dependent SHG response of the nanohole arrays was measured by rotating the polarization direction of the pumping laser with H2. The polarization properties of the emitting SHG signal was analyzed by a Glan-laser polarizer (H4).

Figure 6(b) presents one of the nonlinear emission spectra of the cross-shaped nanohole arrays with a broad measurement range from 350 to 700 nm. The nonlinear emission spectrum shows a narrowband emission at the second harmonic of the pump wavelength 395 nm and a weak two-photon photoluminescence (TPPL) at 550 nm, as well as a broadband white-light supercontinuum (WLC) that extends to the limit of our detection window (~700 nm). The SHG and WLC signal intensities are proved to be second- and fourth-power of the incident light intensity from Figs. 6(c) and 6(d), respectively.

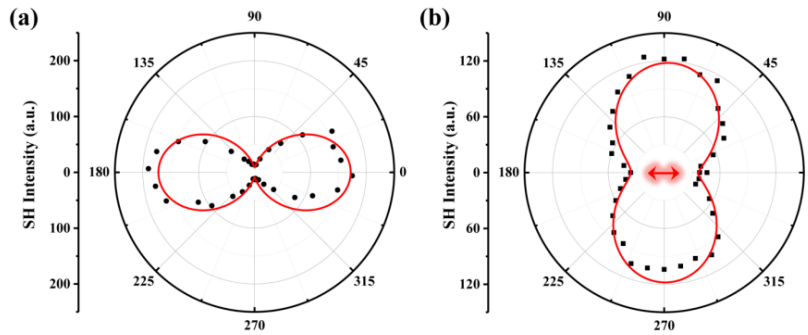## A2. Polarimetric analysis of the SHG signal in the cross-shaped nanohole

Fig. 7. (a) Experimental polar plot for the measured SHG intensity at l = 95 nm as a function of the polarization angle of the pumping laser, where 0°represents x-polarized pumping; (b) The polarimetric analysis of the SH emissions in the nanohole arrays at l = 95 nm under a fixed pumping polarization along x-axis.

Polarization-dependent measurements were performed to address the second-order nonlinear susceptibility tensor $\chi^{(2)}$ properties. For the cross-shaped geometry, it reduces to C_{1v} when the substrate-air asymmetry is taken into account. The only in-plane nonzero tensor elements for those symmetries are $\chi^{(2)}$ yyy, $\chi^{(2)}$ yxx, $\chi^{(2)}$ xyx and $\chi^{(2)}$ xxy, where the first index represent the SHG polarization and the latter two indices represent the polarizations of the two incident fields [17]. In Fig. 7(a), it presents measured SHG intensity at l = 95 nm as a function of the polarization angle of the pumping laser, where 0°represents x-polarized pumping. One can see clearly that the SHG intensity under x-polarized pumping is remarkably larger than that under y-polarized pumping. It can be attributed to the asymmetric local-field distributions, as well as

the near-resonance enhancement effect for *x*-polarized pumping. For *y*-polarized pumping, the centrosymmetric local-field distribution with an off-resonance condition leads to a nearly vanished SHG efficiency. Furthermore, the polarization of SH emission under a fixed pumping polarization along *x*-axis, is investigated as shown in Fig. 7(b). The results indicate that the *y*-polarized SHG intensity is 3.4 times larger than *x*-polarized one, illustrating the emitted SHG signals are mainly in *y*-polarization. Thus, the element, $\chi(2)$ yxx, plays a dominant role in our experiment.

A3. Calculation of the nonlinear responses of the cross-shaped nanohole

The simulation method is introduced firstly. The linear response of each nanostructure was simulated using the finite-element solver COMSOL [39,40]. A periodic boundary condition was used. The geometry, inferred from high-resolution SEM images, was discretized using an inhomogeneous mesh with the maximal element size being less than 10% of plasmonic wavelength. The dielectric constant of Ag was taken from Handbook of Optical constants of Solids [41]. A uniform dielectric environment of n = 1.44 was used to account for the substrate and 3 nm Cr layer without introducing numerical instabilities. The simulations were performed for normal incidence.
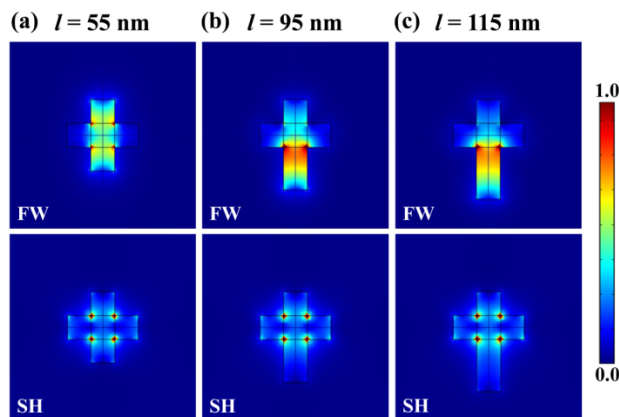

Fig. 8. Calculated fundamental mode and SH mode of three featured nanoholes with (a) *l* = 55 nm, (b) *l* = 95 nm and (c) *l* = 115 nm.

Next, the reciprocity calculations [42] were performed by first exciting the nanostructure with a plane wave at the pump wavelength, then calculating the nonlinear polarization at every point on the nanostructure surface for the second harmonic. Another simulation was then performed by sending in a second wave from the detector at the emission wavelength, i.e. at the SH wavelength. Corresponding fundamental modes and SH modes of three featured nanoholes with *l* = 55 nm, *l* = 95 nm and *l* = 115 nm are shown in Fig. 8. The overlap integral was then performed, thus calculating the eventual SH electric field intensity as shown in Fig. 5(a) of the main text.